Energy loss of charged particles at large distances from metal surfaces

K. Tőkési,[1,2] X.-M. Tong,[3] C. Lemell,[2] and J. Burgdörfer[2]
[1]*Institute of Nuclear Research of the Hungarian Academy of Sciences, (ATOMKI), H-4001 Debrecen, P.O. Box 51, Hungary, EU*
[2]*Institute for Theoretical Physics, Vienna University of Technology, Wiedner Hauptstrasse 8-10, A-1040 Vienna, Austria, EU*
[3]*Physics Department, Kansas State University, Manhattan, Kansas 66506-2601, USA*

(Received 5 November 2004; published 10 August 2005)

We present a theoretical study of the dissipative component of the force acting on a highly charged ion moving in front of a solid surface at large distances. The friction force (stopping power) of the surface is analyzed employing both the specular-reflection model and time-dependent density functional theory (TDDFT). Contributions from particle-hole and plasmon excitations are discussed. A simple method to include the correction due to the finite width of the plasmon resonance at large wavelength into the TDDFT description of the stopping power is suggested. We present applications to the energy loss of charged particles undergoing distant collisions at grazing incidence angles with the internal surface of the microcapillary. Our results indicate that the correlation between the angular distribution and the energy loss of transmitted ions can be used to probe the dielectric properties of the capillary material at large distances.

DOI: 10.1103/PhysRevA.72.022901 PACS number(s): 34.50.Bw, 79.20.Rf, 71.15.Mb

I. INTRODUCTION

The study of multiply charged ion-solid interactions is of considerable technological importance for the understanding of material damage, surface modification, and plasma-wall interactions. The recent availability of sources for slow highly charged ions (HCI's)—namely, electron cyclotron resonance (ECR) and electron beam ion sources (EBIS)—has led to a flurry of research activities, both experimental and theoretical, in the field of HCI-solid interactions [1–7]. On the most fundamental level, its importance is derived from the complex many-body response of surface electrons to the strong Coulomb perturbation characterized by a large Sommerfeld parameter $\eta_S = Z/v \gg 1$ (Z is the charge and v is the velocity of the incident HCI).

From numerous experimental as well as theoretical studies the following scenario of the HCI-surface interaction has emerged: When an HCI approaches a solid surface, one or more electrons are resonantly captured at large distances (d_c) into high Rydberg states of the projectile. As a result, so-called hollow atoms (ions) are formed where the atomic charge cloud transiently resides in shells with large diameters while the core is virtually empty [8–17]. Direct observation of this short-lived state is complicated by the fact that the ion is always attracted towards the surface by its self-image potential. Consequently it will suffer close collisions upon impact on the surface and the memory of the hollow atom is all but erased. This problem has motivated the study of interactions of HCI's with internal surfaces of microcapillaries and nanocapillaries as an alternative technique to study above surface processes [18–22]. Metal and insulating capillaries have become available at the Tokyo Metropolitan University [23,24], Japan and at the Hahn-Meitner-Institut Berlin, Germany [25,26]. The use of capillary targets allows the extraction of hollow atoms in vacuum. Observation of photons or Auger electrons emitted from them in flight becomes possible. Ions traveling approximately parallel to the capillary axis [Fig. 1(a)] will be attracted by image forces toward the cylindrically shaped internal wall of the capillary [27–32]. When the distance of the ion to the wall reaches a critical value $|\rho_0 - \rho| \leqslant |\rho_0 - \rho_c| = d_c$, resonant charge transfer according to the classical over-the-barrier (COB) model can take place [3,4]. Trajectories of type 2 [Fig. 1(a)] will undergo close collisions with the surface as discussed above, leading to (almost) complete relaxation to the neutral ground state and the loss of memory on the original charge and excitation state. Trajectories of type 3 will undergo only large-distance "above-surface" collisions near the exit edge of the capillary and form hollow atoms and ions due to the electron capture from the surface. These ions can escape prior to hitting the wall and, hence, preserve the memory of the above-surface hollow atom formation.

In this contribution, for sake of simplicity, we focus on the third class of trajectories that will exit without experiencing charge transfer [trajectories of type 1 in Fig. 1(a)] and

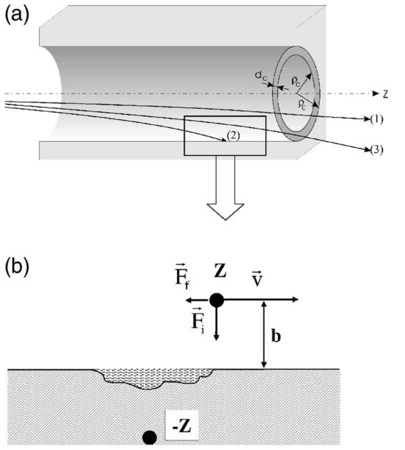

FIG. 1. (a) Sketch of a microcapillary or nanotube with typical ion trajectories. ρ_c is the critical capture radius and d_c is the critical capture distance. (b) Illustration of image ($\vec{F}_i$) and friction force ($\vec{F}_f$) at a distance b from the surface of the projectile moving with velocity $\vec{v}$ parallel to the metal surface.

1050-2947/2005/72(2)/022901(16)/$23.00

presents the dominant fraction of transmitted projectiles. The point of departure of the following analysis is the fact that these ions cruise over a large distance $\gtrsim 1$ μm parallel to the surface in its close proximity ($\lesssim 100$ nm). They may provide a sensitive probe of energy loss at microscopically large distances. Heavy particles as opposed to electrons feature well-defined classical trajectories that allow the determination of the local distance-dependent dielectric response of the surface.

When charged particles are placed in front of the metal surface, electrons in the surface and the bulk will be polarized and build up an induced charge density. This induced charge density can be visualized as an image charge of opposite sign [Fig. 1(b)]. Therefore, the interaction between the charged particle and its image charge is attractive and the particle will be accelerated towards to surface. Due to the image force [$\vec{F}_i$ in Fig. 1(b)], charged particles will eventually always undergo close collisions with the surface even if the initial component of the velocity normal to the surface $\mathbf{v}_\perp$ was zero. When a charged particle is moving with finite parallel velocity $\mathbf{v}_\parallel$ the induced charge density will lag behind the ion, leading to an additional force in the direction opposite to that of the ion velocity [$\vec{F}_f$ in Fig. 1(b)]. This force represents the so-called friction force or stopping power, $S=-dE/dx$. Friction or dissipative forces can thus be visualized in terms of the lateral displacement of the response charge in the direction $-\hat{\mathbf{v}}$. In turn, the latter can be associated with microscopic energy-dissipative processes, the creation of electron-hole pairs, and collective excitations—i.e., surface and bulk plasmons. Energy loss and stopping power near surfaces poses several interesting problems, among them the separation of surface from bulk effects [33–42].

One of the first pioneering treatments of friction forces near surfaces invoked the specular reflection model (SRM) [43–45]. In many applications of ion-surface scattering this simplified classical dielectric response picture has proven to be a very powerful tool. Within the SRM the dielectric response is described by the bulk dielectric function (ε_b) below the surface while above the surface ε is assumed to be given by its vacuum value 1. The presence of the surface is thus represented by a discontinuous ε. The key point of the SRM is that the induced charged density is highly localized on the surface represented by a δ-shaped charge density on the interface. This assumption may lead to the correct representation for the long-range image potential but fails to account the realistic potential distribution in the vicinity of the surface due to the crude description of the induced charge density. The linear-response calculation based on time-dependent density functional theory (TDDFT) [46–50], however, provides a more sophisticated alternative. During the last years, TDDFT has been used for the stopping power in the bulk [51,52]. Olevano and Reining calculated the electron energy loss function of silicon [53] including local-field, self-energy, and excitonic effects. They found a substantial improvement compared with the previous calculations in the description of the experimental spectrum of bulk loss function of silicon for both the peak position and line shape. Very recently the inelastic lifetime of bulk and surface states for noble metals [54,55] have been investigated. It was shown that including the screening of the d electrons into the density functional calculations, the agreement between the experimental and theoretical values is improved. For a jellium surface, only very few calculations have been performed for energy loss near surfaces [56,57]. Cazalilla and Garcia de Abajo [58] have shown that at low velocities and in the vicinity of the surface the stopping power is significantly larger calculated within the framework of TDDFT than the SRM. So far, an investigation of the stopping power at large distances within the framework of TDDFT is not available.

In this paper we provide a comparative analysis of the friction force for charged particles within the framework of the SRM and TDDFT with the emphasis on large distances from the surface. We will treat the problem in TDDFT at the level of the local-density approximation (LDA) and the random phase approximation (RPA). The contributions of particle-hole and plasmon excitations are considered separately. We will suggest an improved description of the stopping power based on our density functional calculations that includes plasmon decay and is applicable at large distances from the surface. Furthermore, we study trajectories of type 1 [see Fig. 1(a)] that do not undergo charge exchange, but come close enough to the walls to suffer a significant energy loss. It is worth noting that the present proposal resembles the measurement of electron energy loss in grazing collisions with crystals using the technique of reflection high-energy electron diffraction (RHEED) [59] and the measurement of ion energy loss in collisions between ions and surface steps [60].

We perform the simulations for Al and protons with energy of to 2.1 keV/amu as projectiles and for Ni and Kr^{30+} ions with energy of to 2.5 eV/amu as projectiles. We note, however, the resulting energy loss is much larger for higher charge of the incident projectile. At low energies, the stopping power depends linearly on the projectile velocity [51,61]. Therefore we will show the stopping power data scaled by the projectile velocity.

In our investigations the linear response theory is used. We note, however, that the applicability of linear-response theory to the present case of slow charged particle with $Z/v \gg 1$ is *a priori* not obvious. Its justification is based on the quasistatic limit of weak perturbations at large distances rather than on short interaction times as implied by $Z/v<1$. Simple estimates [4] indicate that for distances $d > r_s\sqrt{Z}$ nonlinear effects should still be weak where r_s is the Wigner-Seitz radius. The distant ion-capillary surface interactions should therefore be well approximated by the linear response. Throughout the paper atomic units are used unless stated otherwise.

II. THEORETICAL BACKGROUND

We briefly review the theoretical framework for the dielectric response of surfaces which provides the starting point for our investigations of energy loss and stopping at large distances.

A. Surface response function

The response of a many-body system to an external perturbation is one of the key quantities of interest in many-body physics. When the response is treated within perturbation theory to first order (linear response) the corresponding response function can be determined quite accurately for a large class of systems. For many-body systems of charged particles such as quasifree electrons of a metal interacting with an electric field set up by an external charge, the response function is usually expressed in terms of the (bulk) dielectric constant $\varepsilon_b(\vec{q},\omega)$:

$$\varepsilon_b(\vec{q},\omega) = \frac{\rho_{\text{ext}}(\vec{q},\omega)}{\rho(\vec{q},\omega)}, \tag{1}$$

where ρ_{ext} is the external charge causing the dielectric displacement while ρ includes both ρ_{ext} and the induced displacement charge ρ_{ind} in the medium. This definition taken from classical electrodynamics turns out to be the inverse of the dielectric response function for charged particle systems whose exact expression can be found in books on many-body theory [62]:

$$\frac{1}{\varepsilon(\vec{q},\omega)} - 1 = \frac{4\pi}{q^2}\chi(\vec{q},\omega). \tag{2}$$

The right-hand side of Eq. (2) is denoted by $\chi(\vec{q},\omega)$, the response function. Equation (2) represents the dynamic (i.e., frequency ω and wave number $\vec{q}$ dependent) polarizability of the medium. This expression as functions of $\vec{q}$ and ω is valid for systems which are translationally invariant with respect to both position $\vec{r}$ and time t. The charge density fluctuation is space and time dependent with Fourier components $\rho(\vec{q},\omega)$. For isotropic systems, ε will depend only on the magnitude of $|\vec{q}|=q$ and ω. Equation (2) is directly applicable only for homogeneous systems such as bulk solids when the lattice structure can be neglected (e.g., "jellium").

Due to the breaking of translational symmetry in the direction of the surface normal $(\hat{z})$, the response function becomes nonlocal in z while retaining its dependence on the wave vector in the plane of the surface. The dielectric response theory for the bulk requires therefore modifications near surfaces. In order to motivate the nonlocal generalization of χ we express χ in terms of the induced density ρ_{ind} as

$$\rho_{\text{ind}}(q,\omega) = \chi(q,\omega)\Phi_{\text{ext}}(q,\omega), \tag{3}$$

where $\Phi_{\text{ext}}(q,\omega)$ is the three-dimensional Fourier transform of a Coulomb potential. The extension of Eq. (3) to the case of broken translational invariance along the surface normal can now be easily guessed as

$$\rho_{\text{ind}}(Q,\omega,z,b) = \int dz'\,\chi(Q,\omega,z,z')\Phi_{\text{ext}}(Q,\omega,z',b), \tag{4}$$

where b is the z coordinate of the external point charge. In the following three-dimensional vectors are denoted by lowercase $[\vec{p}=(\vec{P},p_z)$ with $p^2=P^2+p_z^2]$ while two-dimensional (2D) vectors in the surface plane are denoted by uppercase letters. In the two-dimensional Fourier representation, the Coulomb potential of an external unit point charge is given by

$$\Phi_{\text{ext}}(Q,\omega,z,b) = \frac{2\pi}{Q}e^{-Q|z-b|}. \tag{5}$$

The response function χ is still local in the Fourier variables (Q,ω) but nonlocal in the coordinate z in which the translational symmetry is broken. In the special case when χ depends only on the coordinate difference $(z-z')$, translational symmetry is restored and Eq. (4) reduces to Eq. (3).

In order to simplify the notation and clarify the underlying general structure of the method we introduce here a convenient Dirac-bracket-type matrix notation with respect to the nonlocal coordinates. Accordingly, ρ_{ind} of Eq. (4) will be identified as a matrix element of the operator $\underline{\underline{\rho}}_{ind}(Q,\omega)$,

$$\rho_{\text{ind}}(Q,\omega,z,z') = \langle z\rangle\underline{\underline{\rho}}_{\text{ind}}(Q,\omega)|z'\rangle, \tag{6}$$

where the induced charge density at the coordinate z is generated by a source located at z'. Analogously, the external potential can be viewed as the matrix elements of the operator $\underline{\underline{\Phi}}_{\text{ext}}(Q,\omega)$,

$$\Phi_{\text{ext}}(Q,\omega,z,z') = \langle z|\underline{\underline{\Phi}}_{\text{ext}}(Q,\omega)|z'\rangle = \frac{2\pi}{Q}\exp(-Q|z-z'|). \tag{7}$$

In this matrix notation Eq. (4) simplifies to

$$\underline{\underline{\rho}}_{\text{ind}}(Q,\omega) = \underline{\underline{\chi}}(Q,\omega)\underline{\underline{\Phi}}_{\text{ext}}(Q,\omega) \tag{8}$$

in complete analogy to Eq. (3).

Within the framework of the "self-consistent field" (SCF) method or RPA we can replace Eq. (8) by

$$\underline{\underline{\rho}}_{\text{ind}}(Q,\omega) = \underline{\underline{\chi}}_0(Q,\omega)\underline{\underline{\Phi}}_{\text{SCF}}(Q,\omega), \tag{9}$$

where χ_0 is the independent particle susceptibility and the self-consistent potential is given by

$$\underline{\underline{\Phi}}_{\text{SCF}}(Q,\omega) = \underline{\underline{\Phi}}_{\text{ind}}(Q,\omega) + \underline{\underline{\Phi}}_{\text{ext}}(Q,\omega). \tag{10}$$

The SCF method takes into account the collective screening by a many-body system. The self-consistency is imposed by requiring ρ_{ind} to satisfy Poisson's equation which takes the form

$$\underline{\underline{\Phi}}_{\text{ind}}(Q,\omega) = \underline{\underline{\Phi}}_{\text{SCF}}(Q,\omega) - \underline{\underline{\Phi}}_{\text{ext}}(Q,\omega) = \underline{\underline{K}}(Q,\omega)\underline{\underline{\rho}}_{\text{ind}}(Q,\omega), \tag{11}$$

where the kernel $\underline{\underline{K}}(Q,\omega)$ in the SCF or RPA is given by the matrix element of the bare Coulomb interaction between electrons:

$$\langle z|\underline{\underline{K}}_{\text{RPA}}(Q,\omega)|z'\rangle = \frac{2\pi}{Q}e^{-Q|z-z'|}. \tag{12}$$

Improvements beyond the RPA can be accomplished, for example, by including exchange-correlation corrections of density functional theory into the kernel,

$$\langle z|\underline{\underline{K}}_{\mathrm{LDA}}(Q,\omega)|z'\rangle = \frac{2\pi}{Q}e^{-Q|z-z'|} + \Phi'_{xc}(n_0(z))\,\delta(z-z'), \tag{13}$$

where

$$\Phi'_{xc}(n_0) = \left.\frac{\delta\Phi_{xc}(n)}{\delta n}\right|_{n=n_0} \tag{14}$$

is the functional derivative taken at the unperturbed, but z-dependent, density $n_0(z)$. Equation (13) corresponds to the LDA. It should be noted that the LDA refers here to the kernel of the self-consistent field equation and not to the exchange-correlation potential in the Kohn-Sham equations for the single-particle orbitals generating χ_0. Combining Eq. (8) and (9) with Eq. (11) we find an operator (integral) equation for the response function $\underline{\underline{\chi}}$,

$$\underline{\underline{\chi}}(Q,\omega) = [1-\underline{\underline{\chi}}_0(Q,\omega)\underline{\underline{K}}(Q,\omega)]^{-1}\underline{\underline{\chi}}_0(Q,\omega), \tag{15}$$

and the corresponding equation for the induced potential:

$$\underline{\underline{\Phi}}_{\mathrm{ind}}(Q,\omega) = \underline{\underline{K}}(Q,\omega)\underline{\underline{\chi}}(Q,\omega)\underline{\underline{\Phi}}_{\mathrm{ext}}(Q,\omega). \tag{16}$$

The starting point for the calculations of the many-body response function $\chi(Q,z,z',\omega)$ is the noninteracting particle density-density correlation function $\chi_0(Q,z,z',\omega)$. An explicit expression for $\chi_0(Q,\omega,z,z')$ can be easily determined within the independent-particle model for the semi-infinite jellium [56]. For later reference we point out that lattice effects and thus coupling to phonons are neglected. Using the Fermi function at zero temperature for the occupation numbers, $f(\vec{p})=\theta(k_f-p)$, $\chi_0(Q,z,z',\omega)$ can be written in terms of the one-electron wave functions and eigenenergies as

$$\chi_0(Q,\omega,z,z') = \sum_{p_z,p_z',\vec{P}}[f(\vec{p}_z)-f(\vec{p}_z{}')] \times\left(\frac{\phi^\star_{p_z}(z)\phi_{p_z}(z')\phi_{p_z'}(z)\phi^\star_{p_z'}(z')}{\omega+w_{p_z}-w_{p_z'}-\vec{Q}\vec{P}-\frac{1}{2}Q^2+i\Gamma}\right), \tag{17}$$

with

$$f(\vec{p}_z) = f(\vec{P},p_z), \quad f(\vec{p}_z{}') = f(\vec{P}+\vec{Q},p_z'). \tag{18}$$

Within the framework of DFT, $\chi_0(Q,\omega,z,z')$ is constructed from Kohn-Sham orbitals $\phi_{p_z}(z)$ [46] with energies w_{p_z} in the degree of freedom along the surface normal. They are self-consistent solutions of

$$\left[-\frac{1}{2}\nabla^2+V_{eff}(z)\right]\phi_{p_z}(z) = w_{p_z}\phi_{p_z}(z), \tag{19}$$

where V_{eff} is the effective potential which depends only on the z coordinate because of translational invariance along the jellium surface and can be written in the LDA as

$$V_{eff}(z) = \Phi(z) + \Phi_{xc}(n[z]), \tag{20}$$

where $\Phi(z)$ is the electrostatic potential which satisfies the Poisson equation and $\Phi_{xc}(n[z])$ is the exchange-correlation potential for which we use the Wigner formula [63]

$$\Phi_{xc}(n) = -\frac{0.611}{r_s(n)} - \frac{0.587^2}{(r_s+7.8)}(r_s+5.85). \tag{21}$$

χ_0 can be rewritten with the help of Green's functions in the form

$$\chi_0(Q,\omega,z,z') = \sum_{\vec{p}} f(\vec{p})\phi^\star_{p_z}(z)\phi_{p_z}(z')[G(z,z',w_+) + G^*(z,z',w_-)], \tag{22}$$

with

$$w_+ = w_k + \omega - \vec{P}\vec{Q} - Q^2/2 + i\Gamma, \tag{23a}$$

$$w_- = w_k - \omega - \vec{P}\vec{Q} - Q^2/2 + i\Gamma. \tag{23b}$$

In principle, Γ should be an infinitesimally small positive number. In practice, we use $\Gamma=0.01$ a.u. in our numerical calculations for reasons of numerical stability. Finally, the integral equation (15) for χ and thus the induced potential are solved by discretization on a grid in z space.

Equation (16) provides the starting point for the calculation of the friction force. The key quantity is the surface loss function $g(Q,\omega)$ related to $\underline{\underline{\Phi}}_{\mathrm{ind}}(Q,\omega)$ as

$$g(Q,\omega) = \frac{Q}{2\pi}e^{2Qb}\langle b|\underline{\underline{\Phi}}_{\mathrm{ind}}(Q,\omega)|b\rangle. \tag{24}$$

The imaginary part of $g(Q,\omega)$ provides the key input to the stopping power calculation.

B. Friction force for particles moving parallel to surfaces

We are interested in calculating the dissipative component of the force acting on the charged projectile with charge Z moving with a velocity parallel to a solid surface ($\vec{v}=V\hat{x}$). We assume that the trajectory is not modified due to the interaction. We also assume that the surface is located in the (x,y) plane. Within the linear-response theory all calculations for the stopping power S can be performed for unit charge $Z=1$ using the scaling

$$S(Z,b,v) = Z^2S(Z=1,b,v) = Z^2S(b,v). \tag{25}$$

From the matrix element of the induced potential—i.e., the surface loss function, the position-dependent friction force, or stopping power—can be written as

$$S(b,V) = -\frac{1}{V}\int\frac{d^2\vec{Q}}{(2\pi)^2}\vec{Q}\vec{V}\,\mathrm{Im}[\langle b|\underline{\underline{\Phi}}_{\mathrm{ind}}(Q,\omega=\vec{Q}\vec{V})|b\rangle], \tag{26}$$

with $Q^2=Q_y^2+\omega^2/V^2$. Equivalently, Eq. (26) can be written in cylindrical coordinates as

$$S(b,V)=-\int_0^{+\infty}dQe^{-2Qb}\int_0^{2\pi}d\phi\cos\phi\frac{Q}{2\pi}\times\mathrm{Im}[g(Q,QV\cos\phi)]. \quad (27)$$

III. SPECULAR REFLECTION MODEL

The specular reflection model pioneered by Ritchie and co-workers [43–45] provides a simplified intuitive model of the surface response while retaining many of the essential physics features of ion-surface scattering.

The dielectric response in the half-space below the surface ($z<0$) is described by the bulk dielectric function $\varepsilon_b(\vec{q},\omega)$ while above the surface ($z>0$)ε is given by its vacuum value 1. This discontinuous change of the dielectric response at the interface models the symmetry breaking due to the presence of a surface within the SRM. Assuming that the parallel (V) and perpendicular (v_z) velocity components of the particle satisfy the relation $V\gg v_z$, the induced potential per unit charge at position $\vec{r}$ is given by [64,65]

$$\Phi_{\mathrm{ind}}(\vec{R},r_z,b,\omega)=\frac{1}{2\pi}\int\frac{d\vec{Q}}{Q}e^{i\vec{Q}\cdot\vec{R}}[\Phi^{(1)}+\Phi^{(2)}], \quad (28)$$

with

$$\Phi^{(1)}=\Theta(b)\Theta(r_z)\frac{\varepsilon_s(Q,\omega)-1}{\varepsilon_s(Q,\omega)+1}e^{-Q(r_z+b)}, \quad (29)$$

$$\Phi^{(2)}=\Theta(b)\Theta(-r_z)\frac{2\varepsilon_s(Q,r_z,\omega)}{\varepsilon_s(Q,\omega)+1}e^{-Qb}, \quad (30)$$

where $\vec{r}=(\vec{R},r_z)$, $\omega=\vec{V}\vec{Q}$, and $\Theta(x)$ is the Heaviside step function. The terms $\Phi^{(1)}$ and $\Phi^{(2)}$ refer to the region of the electronic coordinate above and below the surface. The projectile is assumed to be above the surface ($b>0$). Equation (27) is expressed in terms of the surface dielectric function [45,66]

$$\varepsilon_s(Q,z,\omega)=\frac{Q}{\pi}\eta(Q,z,\omega), \quad (31)$$

where

$$\eta(Q,z,\omega)=\int_{-\infty}^{\infty}\frac{dq_ze^{iq_zz}}{(Q^2+q_z^2)\varepsilon_b(q,\omega)}. \quad (32)$$

In the following, we will use the simplified notation $\eta(Q,\omega)=\eta(Q,z=0,\omega)$ for its value at $z=0$. From Eq. (28) we can directly identify the Fourier component of the induced potential

$$\langle r_z|\underline{\underline{\Phi}}_{\mathrm{ind}}(Q,\omega)|b\rangle=\Phi_{\mathrm{ind}}(Q,r_z,b,\omega)=\frac{2\pi}{Q}[\Phi^{(1)}+\Phi^{(2)}], \quad (33)$$

with diagonal elements

$$\langle b|\underline{\underline{\Phi}}_{\mathrm{ind}}(Q,\omega)|b\rangle=\frac{2\pi}{Q}\frac{\varepsilon_s(Q,\omega)-1}{\varepsilon_s(Q,\omega)+1}e^{-2Qb}. \quad (34)$$

Consequently, the surface loss function in the SRM reduces to

$$g_{SRM}(Q,\omega)=\frac{\varepsilon_s(Q,\omega)-1}{\varepsilon_s(Q,\omega)+1}. \quad (35)$$

For later reference we introduce here another response function $\bar{\varepsilon}$, not to be confused with ε_s, as

$$\frac{1}{\bar{\varepsilon}(Q,\omega)}-1=\frac{2\pi}{Q}\int_{-\infty}^{+\infty}dz\int_{-\infty}^{+\infty}dz'\chi(Q,z,z'\omega). \quad (36)$$

Its significance is derived from the fact that it contains both bulk- and surface-specific contributions to the dielectric response. Within the SRM, when bulk excitations are also included, Eq. (36) becomes

$$\frac{1}{\bar{\varepsilon}(Q,\omega)}=\frac{\varepsilon_s(Q,\omega)-1}{\varepsilon_s(Q,\omega)+1}-\frac{1}{\varepsilon_b(Q,q_z=0,\omega)}. \quad (37)$$

There is a wide variety of models of bulk dielectric functions available that can be used to determine $g_{SRM}(Q,\omega)$ via Eqs. (31)–(35). Benchmarks of a numerically satisfactory description are (a) the correct optical photoabsorption limit ($\sim\mathrm{Im}\{\varepsilon_b^{-1}(q=0,\omega)\}$), (b) the correct asymptotic free-particle dispersion $\sim q^2/2$ for $q\gg1$, (c) the correct dispersion relation for bulk plasmons at small q, and (d) the correct width (or damping) of the plasmon peak.

Ferell *et al.* [67] suggested an approximate form

$$\varepsilon_b(q,\omega)=1+\frac{\omega_p^2}{s^2q^2-i\pi\omega s^2q\theta(2q_F-q)/2q_F-\omega(\omega+i\gamma)}, \quad (38)$$

where $\omega_p=\sqrt{(3/r_s^3)}$ is the classical bulk plasmon frequency, r_s is the Wigner-Seitz radius, and γ is the damping of collective excitation. In Eq. (38), s denotes the group velocity of the plasmons at small wave numbers. From the Lindhard dielectric function [68] we expect

$$s=q_F/\sqrt{3}. \quad (39)$$

Further improvements can be built into Eq. (38) by choosing

$$\varepsilon_b(q,\omega)=1+\frac{\omega_p^2}{s^2q^2+q^4/4-i\pi\omega s^2q\theta(x_1)\theta(x_2)/2q_F-\omega[\omega+i\gamma(q)]}, \quad (40)$$

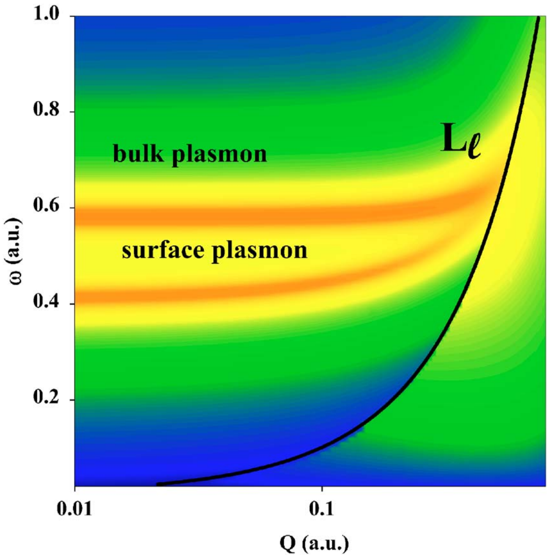

FIG. 2. (Color online) Gray scale plot (white, minimum intensity; black, maximum intensity) of the energy loss function $\mathrm{Im}[-1/\bar{\varepsilon}(Q,\omega)]$ [Eq. (37)] for Al based on SRM calculations using he hydrodynamic model for s. The line indicates the border $L_\ell = qq_F + q^2/2$ where the channel for particle-hole excitation opens.

where $x_1 = \omega - q^2/2 + q_F q$ and $x_2 = q^2/2 + q_F q - \omega$. These cutoffs conform with the energy-momentum dispersion of a free particle $\sim q^2/2$. Moreover, we allow for a momentum-dependent damping $\gamma(q)$ [69,70]. Explicit expressions for $\gamma(q)$ can be obtained from fits to experimental data. For the case of Al, measurements for the broadening of the bulk plasmon loss peak as a function of q have been reported [71,72] and can be represented by

$$\gamma(q) = \gamma_0 + \gamma_2 q^2 + \gamma_4 q^4, \tag{41}$$

with $\gamma_2 = 0.0148$ a.u. and $\gamma_4 = 0.765$ [71]. In our numerical studies we will use $r_s = 2.07$ and $\gamma_0 = 0.03$ a.u. for Al.

Figure 2 displays the density plot of the excitation spectrum—i.e., $\mathrm{Im}\{-\bar{\varepsilon}(Q,\omega)^{-1}\}$ [see Eq. (37)]—using ε_b as given by Eq. (40) for Al. The bulk and surface plasmon dispersion can be clearly seen. The solid line L_ℓ in Fig. 2 indicates the onset of the continuum. The region of small ω predominantly contributes to the stopping power at large distances from the surface. With increasing momentum transfer Q, both the surface and bulk plasmon peaks shift to higher energies. The dispersion of plasmon peaks is controlled by s. A negative dispersion as discussed in [56] is not reproduced in the SRM for Al.

Using the abbreviations

$$a = s^2 q^2 - \omega^2 + q^4/4, \tag{42}$$

$$d = \frac{\pi s^2 q\, \theta(x_1)\, \theta(x_2)}{2 q_F}, \tag{43}$$

the surface dielectric function can be expressed as

$$\eta(Q,\omega) = A - i(B + C), \tag{44}$$

where

$$A = \int_{-\infty}^{\infty} dq_z \left\{ \frac{a(a+\omega_p^2) + \omega^2(\gamma+d)^2}{q^2[(a+\omega_p^2)^2 + \omega^2(\gamma+d)^2]} \right\}, \tag{45a}$$

$$B = \int_{-\infty}^{\infty} dq_z \left\{ \frac{\omega\omega_p^2\gamma}{q^2[(a+\omega_p^2)^2 + \omega^2(\gamma+d)^2]} \right\}, \tag{45b}$$

$$C = \int_{-\infty}^{\infty} dq_z \left\{ \frac{\omega\omega_p^2 d}{q^2[(a+\omega_p^2)^2 + \omega^2(\gamma+d)^2]} \right\}, \tag{45c}$$

which leads to a surface loss function

$$\mathrm{Im}\{g_{SRM}(Q,\omega)\} = -\frac{2\tilde{B}}{(\tilde{A}+1)^2 + (\tilde{B}+\tilde{C})^2} - \frac{2\tilde{C}}{(\tilde{A}+1)^2 + (\tilde{B}+\tilde{C})^2}, \tag{46}$$

with $\tilde{A} = QA/\pi$, $\tilde{B} = QB/\pi$, and $\tilde{C} = QC/\pi$. The terms $\tilde{B}$ and $\tilde{C}$ are associated with the plasmon and particle-hole damping, respectively. Ignoring for the moment the fact that in the denominator both $\tilde{B}$ and $\tilde{C}$ appear and thus these contributions are mixed, we can write Eq. (46) as

$$\mathrm{Im}\{g_{SRM}(Q,\omega)\} = \mathrm{Im}\{g_{SRM}^{pl}(Q,\omega)\} + \mathrm{Im}\{g_{SRM}^{ph}(Q,\omega)\}. \tag{47}$$

We refer to $\mathrm{Im}\{g_{SRM}^{pl}(Q,\omega)\}$ and $\mathrm{Im}\{g_{SRM}^{ph}(Q,\omega)\}$ as the surface loss functions due to the collective plasmon excitations and due to the particle-hole excitations, respectively. At large distances from the surface, the dominant contribution to the loss arises from small momentum ($Q \ll 1$) and energy transfers ($\omega \ll 1$). Therefore we can determine the asymptotic form of Eq. (47) by neglecting all terms in first order in ω^2 [44]. In this case an unambiguous separation can be achieved between the plasmon and particle-hole excitations

$$\mathrm{Im}\{g_{SRM}^{pl}(Q,\omega)\} = -\frac{2\tilde{B}}{(\tilde{A}+1)^2}, \tag{48}$$

$$\mathrm{Im}\{g_{SRM}^{ph}(Q,\omega)\} = -\frac{2\tilde{C}}{(\tilde{A}+1)^2}. \tag{49}$$

In this limit analytic expressions can be derived for the stopping power [44]. By contrast we refer in the following to Eq. (46) as the numerical solution of the SRM model.

A. Plasmon excitation

In the long-wavelength limit of plasmon excitations we find

$$\mathrm{Im}\{g_{SRM}^{pl}(Q,\omega)\} = -\frac{2\tilde{B}}{(\tilde{A}+1)^2} = -2\frac{Q}{\pi}\frac{1}{(\tilde{A}+1)^2}\frac{\omega\gamma q_{TF}^4}{\omega_p^2}\delta, \tag{50}$$

with $q_{TF} = (12/\pi)^{1/3}/\sqrt{r_s}$ being the Thomas-Fermi wave vector and

$$\delta = \int_{-\infty}^{\infty} \frac{dq_z}{(q_z^2+Q^2)(q_z^2+Q^2+q_{TF}^2)^2} = \pi\left[\frac{1}{q_{TF}^4 Q} - \frac{2Q^2+3q_{TF}^2}{2q_{TF}^4(Q^2+q_{TF}^2)^{3/2}}\right]. \tag{51}$$

The stopping power is, in the limit of large distances $b \gg 1$, determined by the $Q \to 0$ limit

$$\lim_{Q\to 0}[-\operatorname{Im}\{g_{SRM}^{pl}(Q,\omega)\}] = \omega\frac{2\gamma_0}{\omega_p^2}. \tag{52}$$

Inserting Eq. (52) into Eq. (26) leads to

$$S_{SRM}^{pl} = \frac{2\gamma}{\pi V^2 \omega_s^2}\int_0^{\infty} d\omega\omega^2 K_0(2b\omega/V) = \frac{\gamma V}{8\omega_s^2}\frac{1}{b^3}, \tag{53}$$

where $\omega_s = \omega_p/\sqrt{2}$ is the classical surface plasmon frequency and K_0 is the modified Bessel function of second kind.

Generalizing the observation that at small Q and ω values the term of the loss function associated with plasmon excitation is linearly depend on the frequency [see Eq. (52)] we can write

$$\operatorname{Im}\{-g_{SRM}^{pl}(Q,\omega)\} = \omega F_{SRM}^{pl}(Q,V). \tag{54}$$

Figure 3(a) shows the surface loss function given by the numerical solution of the SRM model. The linear dependence is fulfilled approximately for $\omega \lesssim 0.01$ a.u. However, if $\omega > 0.01$ a.u., higher-order contributions in the dielectric function become non-negligible and the linear dependence ceases to be valid. $F_{SRM}^{pl}(Q,V)$ can be fitted to the form

$$F_{SRM}^{pl}(Q,V) = a_{SRM}^{pl}(V)e^{-c_{SRM}^{pl}(V)Q}, \tag{55}$$

with

$$a_{SRM}^{pl}(V) = 2\gamma V/\omega_p^2. \tag{56}$$

Using the functional form, Eq. (55), the integrals in Eq. (26) can still be calculated analytically and the stopping power becomes

$$S_{SRM}^{pl} = \frac{\gamma V}{8\omega_s^2}\frac{1}{(b+c_{SRM}^{pl})^3}. \tag{57}$$

We note for later reference that a similar asymptotic form can be derived from a Taylor expansion of the loss function $g(Q,\omega)$, keeping only the leading order terms in Q. Figure 3(b) displays the stopping power contribution originating from plasmon excitation. About 100 a.u. from the surface the asymptotic form [Eq. (53)] agrees very well with the numerical solution of the SRM and describes the stopping power very accurately. However, at smaller distances discrepancies indicate that contributions from shorter wavelengths become important.

B. Particle-hole excitation

In the long-wavelength limit, the contribution from particle-hole excitation can be written as

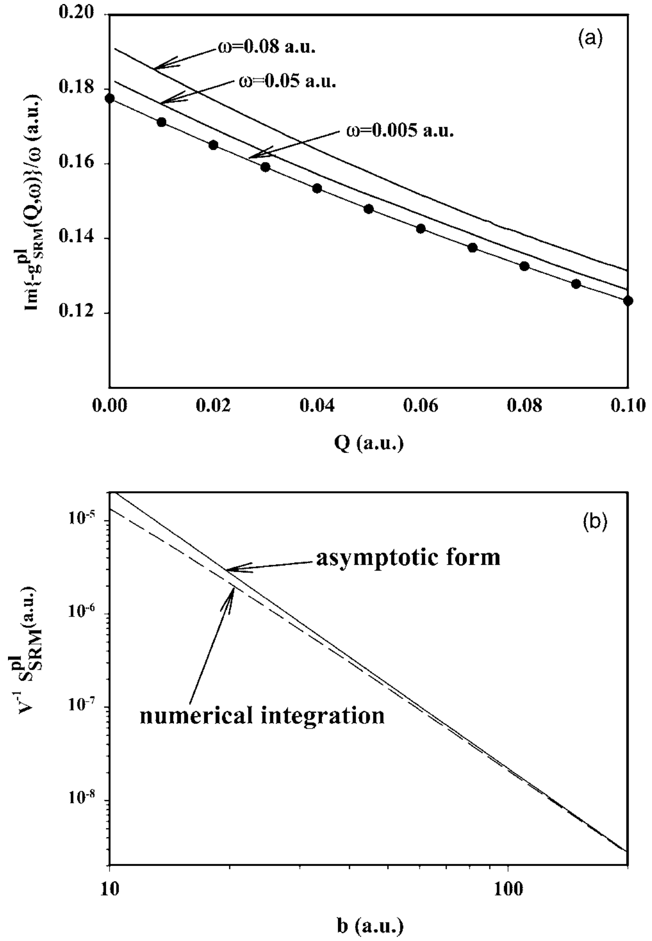

FIG. 3. (a) Surface loss function divided by the frequency for plasmon excitation as a function of momentum transfer Q for various ω within the SRM. Solid line: direct numerical integration of Eq. (46). Circle: fit with $F_{SRM}^{pl}(Q) = a_{SRM}^{pl}\exp(-c_{SRM}^{pl}Q)$. (b) Stopping power contribution due to the plasmon excitation, S_{SRM}^{pl}. Dashed line: direct integration using the surface loss function, Eq. (46). Solid line: long-wavelength limit given by Eq. (48).

$$\operatorname{Im}\{g_{SRM}^{ph}(Q,\omega)\} = -\frac{2\tilde{C}}{(\tilde{A}+1)^2} = -2\frac{Q}{\pi}\frac{1}{(\tilde{A}+1)^2}2\omega\alpha, \tag{58}$$

with

$$\alpha = \int_{-\sqrt{4k_F^2-Q^2}}^{\sqrt{4k_F^2-Q^2}} \frac{dq_z}{\sqrt{q_z^2+Q^2}(q_z^2+Q^2+q_{TF}^2)^2}. \tag{59}$$

In the long-wavelength limit $Q \to 0$, Eq. (58) reduces to

$$\lim_{Q\to 0}[-\operatorname{Im}\{g_{SRM}^{ph}(Q,\omega)\}] = \omega\frac{4Q}{\pi q_{TF}^4}\ln\left[\frac{1}{u^2}\frac{4u_m^2}{u_m^2+1}\right], \tag{60}$$

with $u = Q/q_{TF}$ and $u_m = 2k_F/q_{TF}$. Inserting Eq. (60) into Eq. (26) the particle-hole contribution to stopping follows as

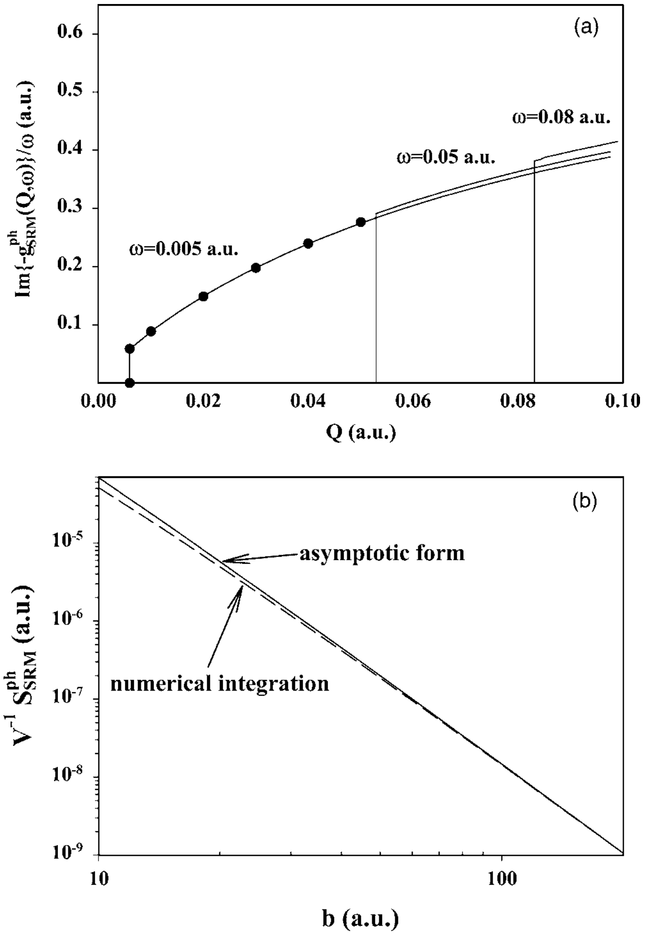

FIG. 4. (a) Surface loss function divided by the frequency for particle-hole excitation as a function of momentum transfer Q for various ω within the SRM. Solid line: direct numerical integration with Eq. (46). Circle: fit with $F^{ph}_{SRM}(Q)=a^{ph}_{SRM}Q\ln(c^{ph}_{SRM}/Q)\theta[Q-Q_l(\omega)]$. (b) Stopping power contribution due to the particle-hole excitation, S^{ph}_{SRM}. Dashed line: direct integration using the surface loss function described by Eq. (46). Solid line: long-wavelength limit given by Eq. (49).

$$S^{ph}_{SRM}=\frac{3V\ln(0.983q_{TF}b)}{2\pi q^4_{TF}}\frac{1}{b^4}. \tag{61}$$

In general, the particle-hole contribution to the surface loss function, $\mathrm{Im}\{-g^{ph}_{SRM}(Q,\omega)\}$, can be written in analogy to Eq. (54) as

$$\mathrm{Im}\{-g^{ph}_{SRM}(Q,\omega)\}=\omega F^{ph}_{SRM}(Q,V). \tag{62}$$

Figure 4(a) shows the surface loss function for particle-hole excitation. The linear dependence implied by Eq. (62) is fulfilled for $\omega \lesssim 0.01$ a.u. For larger ω, $\omega > 0.01$ a.u., higher-order contributions in the bulk dielectric function become important. Our numerical calculations can be fitted to the functional form

$$F^{ph}_{SRM}(Q,V)=a^{ph}_{SRM}(V)Q\ln(c^{ph}_{SRM}/Q)\theta[Q-Q_\ell(\omega)], \tag{63}$$

suggested by the analytic structure of $g^{ph}_{SRM}(Q,\omega)$. Also for the particle-hole excitations the asymptotic form can alternatively be found using a Taylor expansion of the loss function, $g(Q,\omega)$ and keeping only the leading-order terms in Q. Figure 4(b) shows the stopping power contribution due to the particle-hole excitation. Above 100 a.u. from the surface the asymptotic form describes the stopping power very accurately while discrepancies arise at smaller distances.

IV. TIME-DEPENDENT DENSITY FUNCTIONAL THEORY

TDDFT has developed in recent years into an attractive alternative to the SRM for calculating the surface response. In this section we investigate its predictions for the surface response and stopping power at large distances. The coordinate-space representation of the matrix element for the induced potential, Eq. (16), reads

$$\Phi_{ind}(Q,z,b,\omega)=\int_{-\infty}^{+\infty}dz'K(Q,z,z')\int_{-\infty}^{+\infty}dz''\chi(Q,z',z'',\omega)\times\Phi_{ext}(Q,z'',b,\omega), \tag{64}$$

where $\chi(Q,z,z',\omega)$ is the first-order many-body response function and

$$K(Q,z,z')=\frac{2\pi}{Q}\exp(-Q|z-z'|)+\delta(z-z')\left.\frac{\partial\Phi_{xc}}{\partial n}\right|_{n=n_0(z)} \tag{65}$$

in the LDA. The first term in Eq. (65) describes the bare Coulomb interaction between electrons, and the second term is the exchange-correlation correction. The scalar electric potential Φ_{ext} due to a charged particle moving parallel to the surface with velocity $\vec{V}$ and at a distance b can be expressed as

$$\Phi_{ext}(Q,z,b,\omega)=\frac{2\pi}{Q}Z\delta(\omega-\vec{Q}\vec{V})e^{-Q|z-b|}. \tag{66}$$

The 2D density plot of the energy loss function $\mathrm{Im}(-1/\bar{\varepsilon})$ [Eq. (36)] of Al within the framework of the LDA (Fig. 5) resembles the two-dimensional distribution given by the SRM (Fig. 2).

Based on the observation that the RPA and LDA approximations to the kernel [Eqs. (12) and (13)] agree with each other, we perform the analytical investigation of the large-distance behavior of the TDDFT stopping power employing the RPA kernel. Details of the calculations can be found in Ref. [73]. Equation (64) can thus be written as

$$\Phi^{RPA}_{ind}(Q,b,b,\omega)=\frac{(2\pi)^2}{Q^2}\int_{-\infty}^{+\infty}dz\int_{-\infty}^{+\infty}dz'e^{-Q|b-z|}\times\mathrm{Im}[\chi(Q,z,z',\omega)]e^{-Q|z'-b|}. \tag{67}$$

With b approaching infinity—i.e., when b is large compared to $z(z')$—we can write

$$\Phi^{RPA}_{ind}(Q,b,b,\omega)=\frac{(2\pi)^2}{Q^2}e^{-2Qb}\int_{-\infty}^{a}dz\int_{-\infty}^{a}dz'e^{Q(z+z')}\times\mathrm{Im}[\chi(Q,z,z',\omega)]. \tag{68}$$

In practice the integration is performed from deep inside the

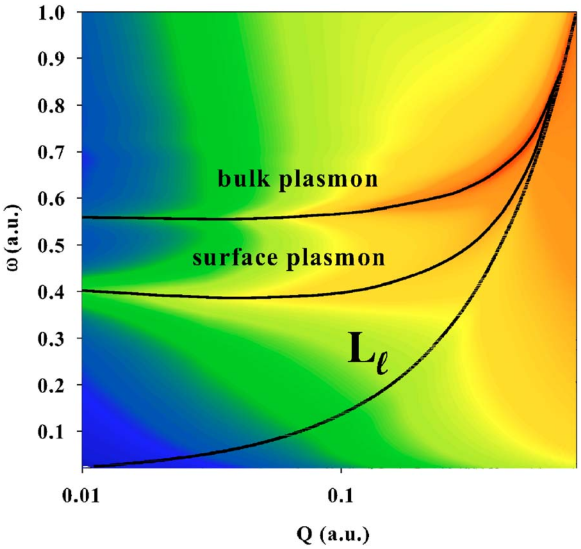

FIG. 5. (Color online) Gray scale plot (white, minimum intensity; black, maximum intensity) of the energy loss function $\mathrm{Im}[-1/\bar{\varepsilon}(Q,\omega)]$ [Eq. (36)] of Al using TDDFT with LDA kernel. The line indicates the border $L_\ell = qq_F + q^2/2$ where the channel for particle-hole excitation opens.

solid to a sufficiently large distance a far from from the surface until convergence is achieved. Substituting Eq. (68) into Eq. (16), the surface loss function in the RPA within the framework of TDDFT reads

$$g_{RPA}(Q,\omega) = \frac{2\pi}{Q}\zeta(Q,\omega), \tag{69}$$

where

$$\zeta(Q,\omega) = \int_{-\infty}^{a}\int_{-\infty}^{a} dz dz' e^{Q(z+z')}\,\mathrm{Im}[\chi(Q,z,z',\omega)]. \tag{70}$$

The large-b behavior can be determined by means of power series expansion in Q around $Q=0$. We note that because of the relation $\omega = \vec{V}\vec{Q}$, the frequency simultaneously approaches zero which requires some care. In order to determine the leading term of Eq. (70), the functions $e^{Q(z+z')}$ and $\chi(Q,z,z',\omega)$ are expanded in a Taylor series. Keeping the leading terms in Eq. (70) and inserting into Eq. (27) leads to

$$S_{RPA}(b,V) = S_{RPA}^{pl}(b,V) + S_{RPA}^{ph}(b,V), \tag{71}$$

where

$$S_{RPA}^{pl}(b,V) = \frac{\pi V}{2} c_{pl} \int_0^{+\infty} dQ Q^2 \exp^{-2Qb}, \tag{72}$$

$$S_{RPA}^{ph}(b,V) = \left[\frac{\pi V}{2} c_{ph}^{(1)} + \frac{3\pi V^3}{24} c_{ph}^{(2)}\right] \int_0^{+\infty} dQ Q^3 \exp^{-2Qb} \tag{73}$$

and

$$c_{pl} = \int_{-\infty}^{+\infty} dz \int_{-\infty}^{+\infty} dz' \left[(z+z') \left.\frac{\partial \chi_i(0,\omega)}{\partial \omega}\right|_{\omega=0} + 2 \left.\frac{\partial^2 \chi_i(Q,\omega)}{\partial Q \partial \omega}\right|_{Q,\omega=0} \right], \tag{74}$$

$$c_{ph}^{(1)} = \int_{-\infty}^{+\infty} dz \int_{-\infty}^{+\infty} dz' \left[(z+z') \left.\frac{\partial \chi_i(0,\omega)}{\partial \omega}\right|_{\omega=0} + 2(z+z')^2 \left.\frac{\partial^2 \chi_i(Q,\omega)}{\partial Q \partial \omega}\right|_{Q,\omega=0} + \left.\frac{\partial^3 \chi_i(Q,\omega)}{\partial^3 \omega}\right|_{\omega=0} \right], \tag{75}$$

$$c_{ph}^{(2)} = \int_{-\infty}^{+\infty} dz \int_{-\infty}^{+\infty} dz' \left[\left.\frac{\partial^3 \chi_i(0,\omega)}{\partial^3 \omega}\right|_{\omega=0} \right]. \tag{76}$$

In Eqs. (74)–(76), $\mathrm{Im}[\chi(Q,z,z',\omega)] = \mathrm{Im}[\chi(Q,z,z',QV\cos\phi)]$ is denoted by $\chi_i(Q,\omega)$. The integrations in Eqs. (72) and (73) can be performed analytically, resulting in the stopping power at large distances:

$$S_{RPA}^{pl}(b,V) = \frac{\pi V}{8} c_p \frac{1}{b^3}, \tag{77}$$

$$S_{RPA}^{ph}(b,V) = \left[\frac{3\pi V}{16} c_{ph}^{(1)} + \frac{3\pi V^3}{64} c_{ph}^{(2)}\right] \frac{1}{b^4}. \tag{78}$$

In analogy with the SRM, we have identified S_{RPA}^{pl} and S_{RPA}^{ph} as the stopping power due to the plasmon and particle-hole excitations, respectively. This assignment originates from the small-Q expansion where terms to the same order in Q can be identified. Its physical justification hinges on the explicit calculation of c_{pl}, $c_{ph}^{(1)}$, and $c_{ph}^{(2)}$. The inevitable discretization errors during the calculations, however, can pose problems when investigating the small-Q limit numerically as Fourier reprocity requires a very wide slab size ($L \approx 2\pi/Q$). In fact this difficulty may have caused spurious results in previous numerical investigations of the surface response function [74]. We therefore combine numerical with analytic techniques in order to explore the small-Q (and large-b) behavior. The starting point is the observation (Fig. 6) that the surface loss function $\mathrm{Im}[g(Q,\omega)]$ divided by the frequency using both the RPA and LDA kernels becomes nearly frequency independent at small values of Q and ω. This linear frequency dependence is fulfilled for both the RPA and LDA when $\omega \lesssim 0.01$ a.u. In analogy to our treatment of the SRM model we assume that the loss function can be written as

$$-\mathrm{Im}\{g_{DFT}(Q,\omega)\} = \omega F_{DFT}(Q,V). \tag{79}$$

In principle, the DFT calculation using either the RPA or LDA kernel contains all excitations—i.e., particle-hole, surface, and bulk plasmon excitations. However, the present jellium calculation predicts that the surface plasmon width decreases linearly with Q as $Q \to 0$ [75–78]. This is due to the fact that the plasmon coupling to the lattice and the plasmon decay into a double electron-hole pair is neglected from the outset. The significance of corrections of the unphysically long lifetimes for long-wavelength plasmon excitations be-

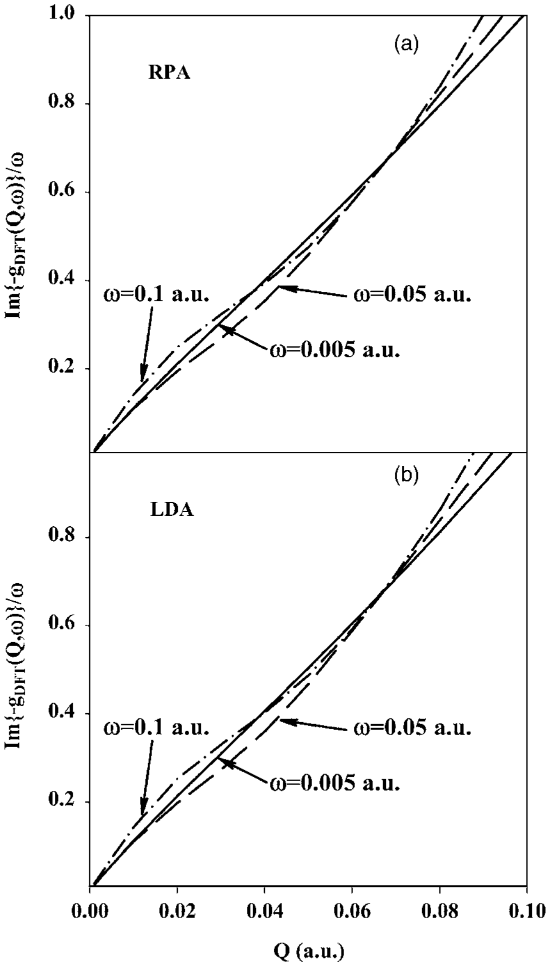

FIG. 6. Surface loss function divided by the frequency as a function of momentum transfer Q with (a) RPA and (b) LDA kernel.

comes obvious when realizing that the asymptotic plasmon contribution within the SRM depends linearly on the $Q \to 0$ value of $\gamma(Q)$. Consequently, the plasmon contribution ($\sim b^{-3}$) to the stopping vanishes in the asymptotic limit $b \to 0$ of DFT for a structureless jellium. Numerically the coefficient c_{pl} is found to be either negligible small or equal to zero. Corrections of this deficiency will be discussed below.

Since the asymptotic contribution to the stopping comes from particle-hole excitations, we fit the numerical data at $\omega = 0.005$ a.u. and $0 < Q < 0.05$ a.u. (Fig. 6) to the functional form [see Eq. (63)]

$$F_{DFT}(Q,V) = a_{DFT}(V) Q \ln(c_{DFT}/Q). \tag{80}$$

Inserting Eqs. (79) and (80) into Eq. (27) the integration with respect to Q can again be done analytically, leading to the stopping power in the form

$$S_{DFT} = \frac{3 a_{DFT} V}{16 b^4}[H_{DFT} + \ln(b)]. \tag{81}$$

This power law closely mirrors the one we found for particle-hole excitation in SRM.

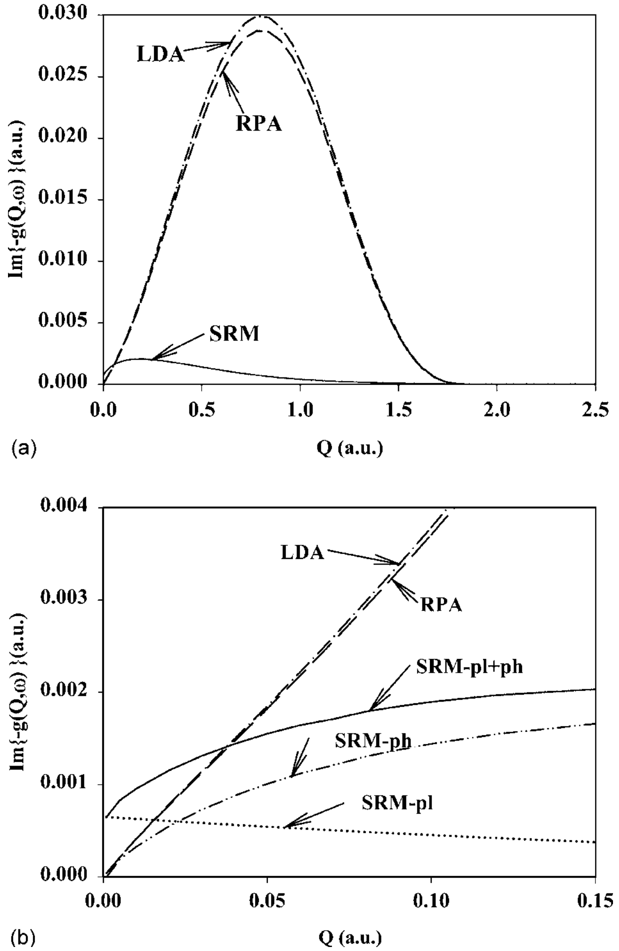

FIG. 7. Surface loss function as a function of momentum transfer Q at $\omega = 0.0037$ a.u. (a) for a wide range of Q and (b) enlarged for the case of small momentum transfers. Dash-dotted line: LDA. Dashed line: RPA. Solid line: SRM and SRM contributions due to plasmon excitation (dotted line) and particle-hole excitation (double-dot-dashed line).

V. COMPARISON BETWEEN SRM AND TDDFT

Figure 7 shows the surface loss function as a function of the momentum transfer Q for $\omega = 0.0037$ a.u. calculated in the framework of the SRM and TDDFT. Almost over the whole range of Q the loss function is significantly larger in DFT than in the SRM [Fig. 7(a)]. Moreover, the loss function is smaller for the RPA kernel than the LDA kernel. This is due to the fact that the effective interaction potential is stronger in the RPA than in the LDA. The exchange correlation term in the LDA reduces the repulsive interaction potential, thereby increasing the polarizability of the surface electron density. The enhancement in the LDA is only about 5% compared to the RPA. We note here that this is in contradiction with the observation of Liebsch [74] where the difference between the LDA and RPA calculations at the peak position is about 60%.

For very small values of Q, however [Fig. 7(b)], the order is reversed: Below the critical value of Q($Q_c \approx 0.04$ a.u.) the loss function within DFT drops to below the SRM value. Decomposing the SRM loss function into its plasmon and

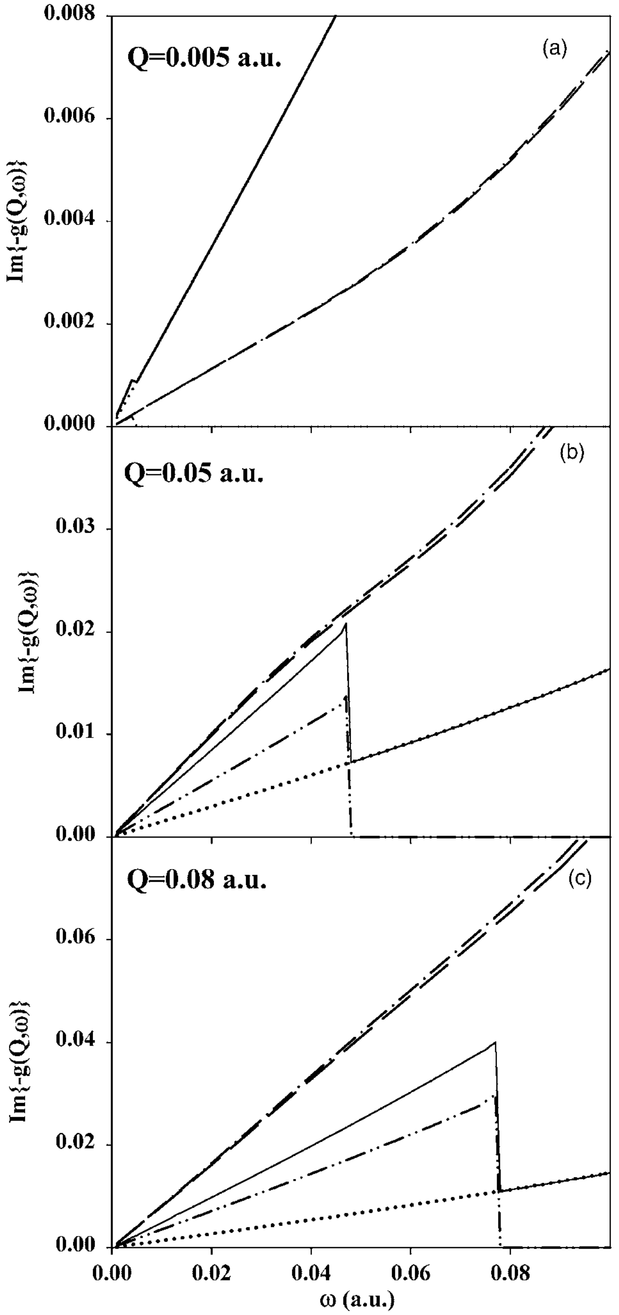

FIG. 8. Surface loss function as a function of frequency for various values of parallel momentum transfer. Dash-dotted line: LDA. Dashed line: RPA. Solid line: SRM and SRM contributions due to plasmon excitation (dotted line) and particle-hole excitation (double-dot-dashed line).

particle-hole contributions clearly indicates that the underestimate of width of the plasmon spectrum at $Q=0$ in TDDFT is the main source for the smaller TDDFT values for Im[$g(Q,\omega)$]. The discrepancy is highlighted in more detail in Fig. 8 where the surface loss functions as a function of frequency for various values of parallel momentum transfer are shown. The transition from the $Q\approx 0$ regime [Fig. 8(a)] where the SRM exceeds the TDDFT value to the regime where particle-hole excitation dominates and thus Im[$g(Q,\omega)$] calculated in TDDFT is larger near $Q\gtrsim 0.04$ [Figs. 8(b) and 8(c)] is clearly seen.

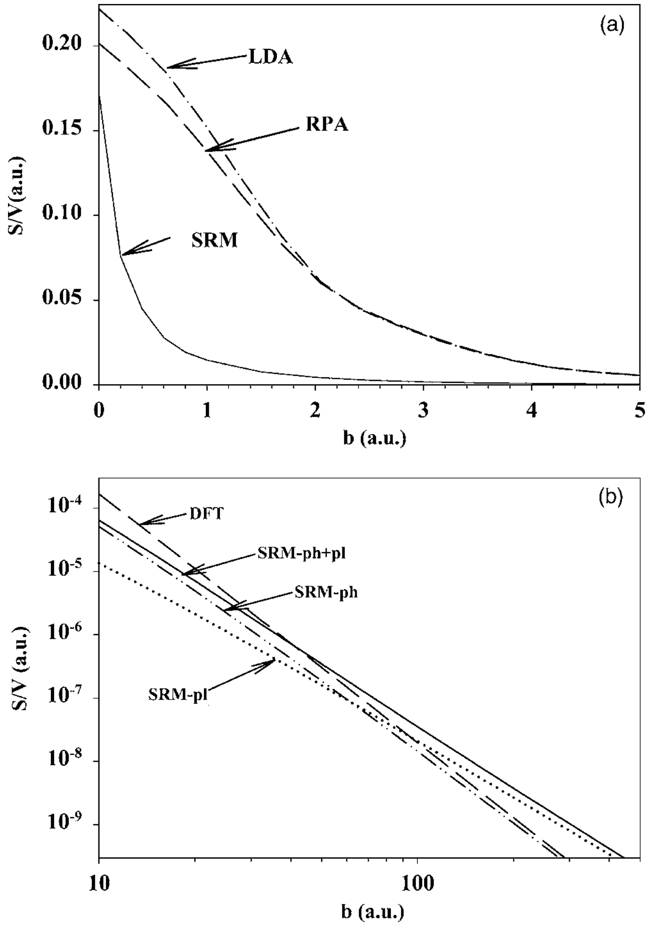

FIG. 9. Distance-dependent stopping power for a unit charge moving on a parallel trajectory in front of the vicinity of an Al surface. (a) Small to intermediate distances (linear scale). Dash-dotted line: LDA. Dashed line: RPA. Solid line: SRM. (b) large distances (log scale). Dashed line: DFT. Solid line: SRM-ph+pl (contributions due to both plasmon and particle-hole excitations). Dotted line: SRM-pl (contribution due to plasmon excitation). Double-dot-dashed line: SRM-ph (contribution due to particle-hole excitation).

Finally, the distance-dependent stopping power, Eq. (27), near an Al surface with parallel velocity is presented both for small to intermediate distances [Fig. 9(a)] and large distances [Fig. 9(b)]. The stopping power is scaled by the projectile velocity. Our present calculations confirm the observation by Cazalilla and Garcia de Abajo [58] that at low velocities and in the vicinity of the surface large differences between the stopping power calculated within the framework of TDDFT and the one calculated with the SRM exist. The latter decreases faster with increasing distance than the former. This behavior directly mirrors the surface loss function at intermediate to large values of Q [see Figs. 8(b) and 8(c)]. Also the results for the RPA and LDA kernels reflect the corresponding differences between Im[g_{DFT}^{RPA}] and Im[g_{DFT}^{LDA}]. At large distances [Fig. 9(b)] a completely different situation emerges. The stopping powers for RPA and LDA kernels are virtually indistinguishable (labeled as DFT) and fall below the value of the SRM at about ≈40 a.u. Obviously, this transition is related to the dominance of the plasmon contribution near $Q=0$ missing in TDDFT because of the incorrect width of the plasmon resonance at small Q.

VI. APPLICATIONS

A. Improvement of TDDFT at large distances

The asymptotic analysis of the large-distance behavior of the stopping power immediately suggests remedies for the TDDFT as applied to a jellium surface. The underestimate of the width $\gamma(Q)$ of the plasmon line near $\omega_s(Q\approx 0)$ leads to an underestimate of the surface loss function near $\mathrm{Im}g(Q\approx 0,\omega\approx 0)$. With Q approaching zero, energy and momentum conservation cannot be satisfied in the absence of the lattice for the decay of a plasmon into a single particle-hole excitation. At long wavelengths $Q<Q_{ph}$, where Q_{ph} is the wave number where the plasmon dispersion merges into the continuum of particle-hole excitations, plasmons do not suffer Landau damping. The energy conservation for the single particle-hole decay reads

$$\omega(Q)=w_{\vec{P}+\vec{Q}}-w_{\vec{P}}=\frac{Q^2}{2}+\vec{P}\vec{Q} \qquad (82)$$

and, therefore,

$$\lim_{Q\to 0}\omega(Q)=0. \qquad (83)$$

It is clear that at small values of Q the decay of plasmons with energy $\omega_s(Q=0)>0$ is suppressed. Ichimaru [79] has shown that the decay rate of the plasmon is proportional to Q^2. Therefore, it vanishes in the long-wavelength limit. The width at $\gamma(Q\approx 0)$ near $Q=0$ is governed primarily by two processes: decay of the plasmon into a particle-hole excitation accompanied by momentum transfer to the lattice (phonons) and emission of pairs of particle-hole excitations [62]. These processes can be taken into account by shifting the plasmon pole in the complex plane near $Q=0$ by an amount given by first-order perturbation theory—i.e., by Fermi's golden rule for these processes. A simplified method to accomplish such a correction is suggested by the behavior of the surface loss function at small Q [see Fig. 7(b)]. Below Q_c the surface loss function calculated within DFT, $\mathrm{Im}[g_{DFT}(Q,\omega)]$, crosses the line $\mathrm{Im}[g_{SRM}(Q,\omega)]$, because of the missing plasmon decay channels. We can simply correct for this deficiency by setting

$$\mathrm{Im}[g^{pl}_{DFT}(Q,\omega)]=\mathrm{Im}[g_{DFT}(Q,\omega)]+\mathrm{Im}[g^{pl}_{SRM}(Q,\omega)]\times\left[1+\exp\left(\frac{Q-Q_c}{Q_{\mathrm{W}}}\right)\right]^{-1}. \qquad (84)$$

In Eq. (84), $\mathrm{Im}[g^{pl}_{SRM}]$ is the plasmon contribution [Eq. (48)] to the SRM and $\mathrm{Im}[g_{DFT}]$ stands for the TDDFT calculations using either the RPA or LDA kernels which give virtually identical results at small Q where the correction applies. The parameters entering Eqs. (84) and (48) can be taken from perturbation theory for interband transitions and correlated two-electron processes. For Al, the critical point for the transition Q_c is at $Q_c\approx 0.04$ a.u. and the transition width is set to $Q_{\mathrm{W}}\approx 0.01$ a.u. Figure 10 displays the position-dependent stopping power, based on DFT corrected for plasmon decay, $\mathrm{Im}[g^{pl}_{DFT}]$, for a unit charge moving along a parallel trajectory in front of an Al surface. This improved form of stopping power including plasmon decay (DFT-pl) significantly exceeds the SRM in the vicinity of the surface while approaching the SRM at large distances.

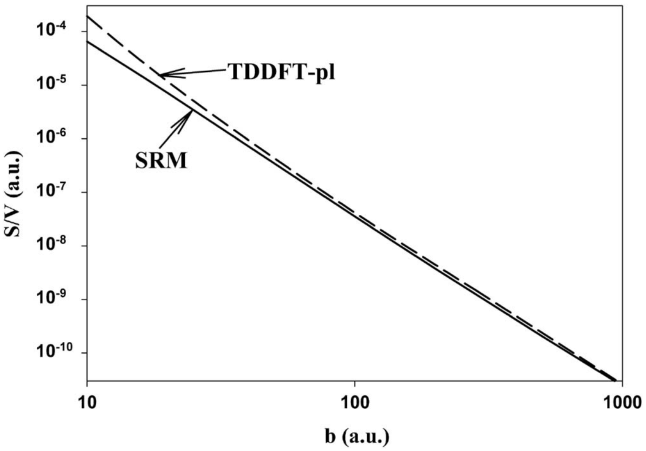

FIG. 10. Distance-dependent stopping power for a unit charge moving in a parallel trajectory in front of an Al surface. Dashed line: DFT-pl. Solid line: SRM.

B. Energy loss of charged particles in capillary transmission

In the following application we first present the energy loss for a proton (H^+) rather than an HCI. The reason for this choice is that for small z differences between TDDFT and SRM are more pronounced. Note, however, that integrated energy loss is much larger and more easily measurable for HCI's. For the study of the problem of energy loss in microcapillary transmission discussed in the Introduction, we have performed a classical trajectory Monte Carlo simulation with an ensemble of 5×10^6 primary trajectories. In our simulations an Al capillary with a radius of 2360 a.u. and length $L=30000$ a.u. was used. The spatial distribution of the ensemble is uniform across the opening of the capillary cylinder. To simulate the spread of the incident beam, we use a Gaussian angular distribution of θ_i with a full width at half maximum (FWHM Δ,θ) of 0.2°. The critical distance of the first capture is taken from the classical-over-the-barrier model [3,4]. Details of the simulation are given elsewhere [32]. For the sake of simplicity, we neglect the curvature of the internal capillary walls. The forces (parallel and perpendicular to the capillary axis) acting on the projectile during the trajectory calculation are therefore close to the surface equivalent to that of a flat surface. In the regime of distances relevant for the energy loss this approximation leads to virtually identical values for flat and curved surfaces. The energy loss of ions that do not undergo capture is restricted to distances larger than the minimum critical distance. According to the COB model [3,4] the estimated distance where the first resonant charge transfer can take place is

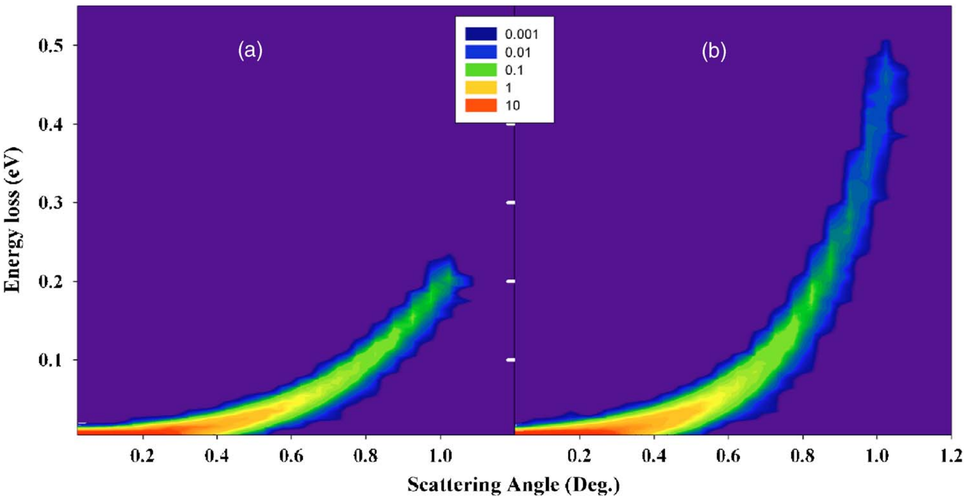

FIG. 11. (Color online) 2D correlation pattern between the energy loss and the scattering angle of H$^+$ ions passing through an Al microcapillary at 2.1 keV/amu energy. (a) Distance-dependent stopping power is calculated by SRM. (b) Distance-dependent stopping power is calculated by DFT-pl.

$$d_c = \frac{\sqrt{2Z}}{W}, \tag{85}$$

where W is the work function of the target. For the case of H$^+$ scattering at an Al capillary with W=4.2 eV, $d_c \approx 9.2$ a.u., and for Kr^{30+} projectiles $d_c \approx 50.2$ a.u. In view of the long interaction times of the ion with the capillary walls ($t \gtrsim 10^6$ a.u.) it is important to estimate the contributions from charge transfer by tunneling at distances larger than d_c. We performed test simulations including tunneling [3,80]. We typically find that despite the long interaction times, the additional tunneling contributions leads only to a slight increase of the effective distance of the capture by tunneling d_T compared to the classical value d_c by $\lesssim$25%. As will be shown explicitly below (see Fig. 14, below), the effect on the resulting energy loss is negligibly small.

The energy loss ($\Delta E = E_f - E_i$, where E_i and E_f are the ion energies at the position of the ion source and detector, respectively) of the charged particle can be obtained from an integration of the friction force (stopping power S) along the trajectory of the particle. According to Fig. 10 the stopping power is negligible small for distances larger than about 100 a.u. from the metallic surface. Most of the ions traveling along trajectories of type 1 [Fig. 1(a)] during the entire transmission will hardly suffer any perceptible energy loss. However, the strength of the stopping power strongly increases as the particle approaches the surface. We introduce the yield function of transmitted ions which have not changed their charge state as

$$Y = \frac{N_{q_i}}{N}, \tag{86}$$

where N_{q_i} is the number of transmitted ions in their initial charge state q_i without undergoing close collisions and N is the total number of primary ions entering the capillary. For protons with v=0.29 a.u. corresponding to 2.1 keV, Y=0.91. We also introduce the energy loss probability density as

$$P(\Delta E) = \frac{N(\Delta E)}{\Delta E N_{q_i}}, \tag{87}$$

where $N(\Delta E)$ is the number of transmitted ions suffering energy loss ΔE. Similarly, we introduce the 2D probability as a function of energy loss ΔE and emission (polar) angle θ as

$$P(\Delta E, \theta) = \frac{N(\Delta E, \theta)}{\Delta E \Delta \theta N_{q_i}}. \tag{88}$$

Figure 11 displays the two-dimensional correlation pattern between the scattering angle and the energy loss employing the SRM [Fig. 11(a)] and DFT-pl [Fig. 11(b)] approximations. In both cases the dominant fraction of the incident beam will undergo only small-angle scattering and will suffer negligible energy loss ($\approx$98% of the transmitted ions). The amount of energy loss is strongly correlated to the distance of closest approach which also determines the strength of the interaction between the projectile and solid surface. We obtain a significantly larger maximum energy loss for DFT-pl than for the SRM. To highlight this effect we integrated the $P(\Delta E, \theta)$ distribution over the scattering angle. Figure 12 shows the energy loss probability for a 2.1 keV/amu H$^+$ ions passing through an Al microcapillary. The energy loss exceeding about 0.3 eV corresponding to $\Delta E/E$=0.014% should be experimentally observable. This would require an energy resolution for the measurement better than $\Delta E/E \approx 0.02$%. We note that with increasing projectile charge the maximum reachable energy loss for DFT-pl approaches the value obtain with the SRM. Since the scattering angle and the distance of closest approach are strongly correlated, the distant-dependent stopping power can be probed in detail.

We turn now to a typical case of a highly charged ion and present results for Kr^{30+} with very low velocity (v =0.01 a.u.) expected to be available at the future HITRAP facility at GSI. Figure 13 shows the two-dimensional correlation pattern between the scattering angle and the energy loss for Kr^{30+} ions with an energy of 2.5 eV/amu employing the SRM approximation for Ni. For Kr^{30+} the first critical capture distance is 40.5 a.u. This minimum distance is large

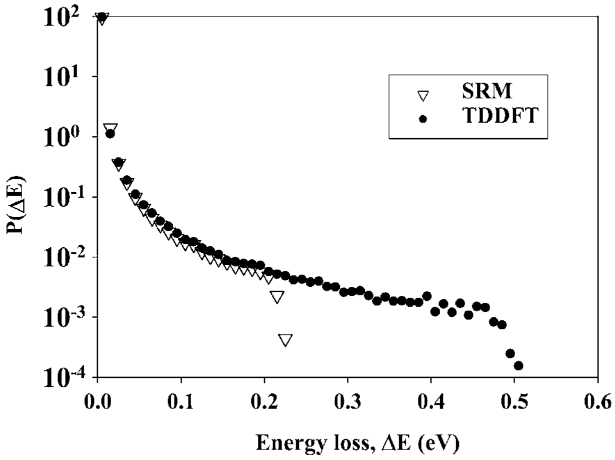

FIG. 12. Energy loss probability for a 2.1 keV/amu H^+ ions passing through an Al microcapillary.

enough that the maximum energy loss for DFT-pl approach should be almost identical to that obtained with the SRM. The maximum energy loss is about 0.9 eV corresponding to $\Delta E/E = 0.4\%$.

Including the contributions due to tunneling increases the effective distance for first capture due to tunneling to $d_T \approx 50$ a.u.—i.e., about 25% larger than the classical value. The point of closest approach without charge transfer is thus shifted further out which results in a decrease in the energy loss. However, the effect of tunneling contributions on the energy loss is very small (see Fig. 14). The reason is that ΔE is an integral quantity over the entire trajectory through the capillary. Since most contributions stem from large distances, the shift in d_c has only a minor effect.

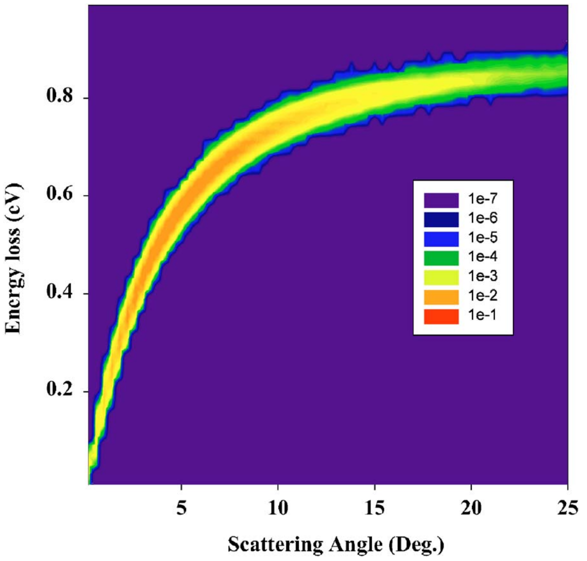

FIG. 13. (Color online) 2D correlation pattern between the energy loss and the scattering angle of Kr^{30+} ions passing through an Ni microcapillary at 2.5 eV/amu energy. The distance-dependent stopping power is calculated by the SRM employing the same bulk dielectric function as in Ref. [32].

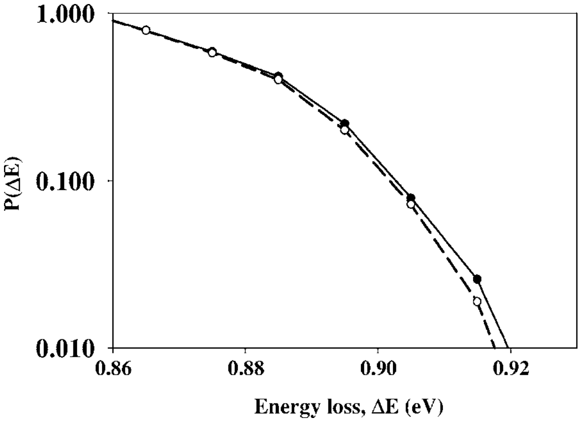

FIG. 14. Energy loss probability for 2.5-eV/amu Kr^{30+} ions passing through a Ni microcapillary. Solid line with full circle: COB model. Dashed line with open circle: COB model with tunneling taken into account.

VII. CONCLUSIONS

In summary, we have presented a detailed investigation of the asymptotic form of the stopping power for charged particles moving parallel to a metal surface at large distances. A comparative study of the linear response employing the specular reflection model and time-dependent density functional theory shows dramatic differences: in the vicinity of the surface the SRM underestimates the stopping power since it underestimates the local electron density that provides the drag force. At large distances, the roles are reversed: the TDDFT calculation for a jellium surface neglecting lattice effects and coupling to phonons underestimates the stopping power. The latter originates from the vanishing (surface) plasmon line width in the long-wavelength limit. Since the SRM contains the experimental linewidth on a phenomenological level, its asymptotic stopping power results in the correct power law $\sim(\text{distance})^{-3}$ and dominates over the TDDFT result $\sim(\text{distance})^{-4}$. We have proposed a simple extension of the TDDFT description that remedies this deficiency. While in the vicinity of the surface this stopping power calculation gives values significantly larger than obtained by SRM, it converges to the SRM in the asymptotic region above the surface. We hope our results will stimulate experimental investigations of the surface dielectric response function at large distances probed by transmission of highly charged ions through microcapillaries or nanotubes [81]. This technique promises the possibility to obtain the surface loss function well separated from the bulk one. It is worth noting that such a proposal resembles the measurement of electron energy loss of electrons transmitted through cylindrical microchannels [82,83]. Higher charges of HCI and better defined classical trajectories should provide a favorable setting for probing the stopping power at large distances. Finally we note, however, in our recent studies, for the sake of simplicity, we restricted ourselves to that type of trajectories which do not suffer charge exchange; trajectories of type 3 [Fig. 1(a)] will give rise to higher energy loss.

ACKNOWLEDGMENTS

The work was supported by the Hungarian Scientific Research Found: OTKA Nos. T038016 and T046095, a grant

"Bolyai" from the Hungarian Academy of Sciences, TéT Grant No. A-15/04, "Stiftung Aktion Österreich-Ungarn," No. 55öu1, the Austrian Fonds zur Förderung der wissenschaftlichen Forschung, FWF (Austria), and EU under Contract No. HPRI-CT-2001-50036. We gratefully acknowledge invaluable inspiration and guidance over many years by our friend and pioneer of this field, Rufus Ritchie.

[1] A. Arnau, F. Aumayr, P. M. Echenique, M. Grether, W. Heiland, J. Limburg, R. Morgenstern, P. Roncin, S. Schippers, R. Schuch, N. Stolterfoht, P. Varga, T. J. M. Zouros, and HP Winter, Surf. Sci. Rep. **27**, 113 (1997).
[2] R. Morgenstern, in *X-Ray and Inner-Shell Processes*, edited by R. L. Johnson, H. Schmidt-Böcking, and B. F. Sonntag, AIP Conf. Proc. No. 389 (AIP, Woodbury, NY, 1997).
[3] J. Burgdörfer, P. Lerner, and F. W. Meyer, Phys. Rev. A **44**, 5674 (1991).
[4] J. Burgdörfer, in *Review of Fundamental Processes and Applications of Atoms and Ions*, edited by C. D. Lin (World Scientific, Singapore, 1993), p. 517.
[5] T. Schenkel *et al.*, Prog. Surf. Sci. **61**, 23 (1999).
[6] F. Aumayr, J. Burgdörfer, P. Varga, and HP Winter, Comments At. Mol. Phys. **34**, 201 (1999).
[7] J. Burgdörfer, in *Scattering and Inverse Scattering in Pure and Applied Science*, edited by E. R. Pike and P. C. Sabatier (Academic Press, London, 2001), p. 1081.
[8] H. Winter, C. Auth, R. Schuch, and E. Beebe, Phys. Rev. Lett. **71**, 1939 (1993).
[9] F. W. Meyer, L. Folkerts, I. G. Hughes, S. H. Overbury, D. M. Zehner, P. A. Zeijlmans van Emmichoven, and J. Burgdörfer, Phys. Rev. A **48**, 4479 (1993).
[10] J. Das and R. Morgenstern, Comments At. Mol. Phys. **29**, 205 (1993).
[11] A. Arnau, R. Köhrbrück, M. Grether, A. Spieler, and N. Stolterfoht, Phys. Rev. A **51**, R3399 (1995).
[12] J. P. Briand, G. Giardino, G. Borsoni, M. Froment, M. Eddrief, C. Sébenne, S. Bardin, D. Schneider, J. Jin, H. Khemliche, Z. Xie, and M. Prior, Phys. Rev. A **54**, 4136 (1996).
[13] C. Lemell, HP Winter, F. Aumayr, J. Burgdörfer, and F. W. Meyer, Phys. Rev. A **53**, 880 (1996).
[14] Q. Yan, D. M. Zehner, F. W. Meyer, and S. Schippens, Phys. Rev. A **54**, 641 (1996).
[15] C. Lemell, J. Stöckl, J. Burgdörfer, G. Betz, HP Winter, and F. Aumayr, Phys. Rev. Lett. **81**, 1965 (1998).
[16] J. J. Ducrée, and F. Casali, U. Thumm, Phys. Rev. A **57**, 338 (1998).
[17] X. M. Tong, D. Kato, T. Watanaba, H. Shimizu, C. Yamada, and S. Ohtani, Phys. Rev. A **63**, 052505 (2001).
[18] Y. Yamazaki, S. Ninomiya, F. Koike, H. Masuda, T. Azuma, K. Komaki, K. Kuroki, and M. Sekiguchi, J. Phys. Soc. Jpn. **65**, 1199 (1996).
[19] Y. Yamazaki, Phys. Scr. **T73**, 293 (1997).
[20] S. Ninomiya, Y. Yamazaki, F. Koike, H. Masuda, T. Azuma, K. Komaki, K. Kuroki, and M. Sekiguchi, Phys. Scr. **T73**, 316 (1997).
[21] S. Ninomiya, Y. Yamazaki, F. Koike, H. Masuda, T. Azuma, K. Komaki, K. Kuroki, and M. Sekiguchi, Phys. Rev. Lett. **78**, 4557 (1997).
[22] Y. Yamazaki, in *Photonic, Electronic and Atomic Collisions*, edited by F. Aumayr and HP Winter, (World Scientific, Singapore, 1998), p. 693.
[23] H. Masuda and K. Fukuda, Science **268**, 1466 (1995).
[24] H. Masuda and M. Satoh, Jpn. J. Appl. Phys., Part 2 **35**, L126 (1996).
[25] N. Stolterfoht, J. H. Bremer, V. Hoffmann, R. Hellhammer, D. Fink, A. Petrov, and B. Sulik, Phys. Rev. Lett. **88**, 133201 (2002).
[26] N. Stolterfoht, J. H. Bremer, V. Hoffmann, R. Hellhammer, Z. D. Pesic, D. Fink, A. Petrov, and B. Sulik, Nucl. Instrum. Methods Phys. Res. B **203**, 246 (2003).
[27] K. Tőkési, L. Wirtz, and J. Burgdörfer, Nucl. Instrum. Methods Phys. Res. B **154**, 307 (1999).
[28] K. Tőkési, L. Wirtz, C. Lemell, and J. Burgdörfer, Phys. Rev. A **61**, 020901(R) (2000).
[29] K. Tőkési, L. Wirtz, C. Lemell, and J. Burgdörfer, Nucl. Instrum. Methods Phys. Res. B **164–165**, 504 (2000).
[30] N. R. Arista and M. A. Fuentes, Phys. Rev. B **63**, 165401 (2001).
[31] N. R. Arista, Phys. Rev. A **64**, 032901 (2001).
[32] K. Tőkési, L. Wirtz, C. Lemell, and J. Burgdörfer, Phys. Rev. A **64**, 042902 (2001).
[33] A. Selloni and R. Del Sole, Surf. Sci. **168**, 35 (1986).
[34] K. Tőkési, D. Varga, L. Köver, and T. Mukoyama, J. Electron Spectrosc. Relat. Phenom. **76**, 427 (1995).
[35] F. Yubero, J. M. Sanz, B. Ramskov, and S. Tougaard, Phys. Rev. B **53**, 9719 (1996).
[36] K. Tőkési, L. Köver, D. Varga, and J. Tóth, Surf. Rev. Lett. **4**, 955 (1997).
[37] M. Vicanek, Surf. Interface Anal. **440**, 1 (1999).
[38] C. M. Kwei, C. Y. Wang, and C. J. Tung, Surf. Interface Anal. **26**, 682 (1998).
[39] S. Tanuma, S. Ichimura, and K. Goto, Surf. Interface Anal. **30**, 212 (2000).
[40] W. S. M. Werner, Surf. Interface Anal. **31**, 141 (2001).
[41] K. Tőkési, X.-M. Tong, C. Lemell, and J. Burgdörfer, Phys. Scr. **T92**, 27 (2001).
[42] G. Gergely *et al.*, Surf. Interface Anal. **33**, 410 (2002).
[43] R. H. Ritchie and A. L. Marusak, Surf. Sci. **4**, 234 (1966).
[44] R. Núñez, P. M. Echenique, and R. H. Ritchie, J. Phys. C **13**, 4229 (1980).
[45] P. M. Echenique, R. H. Ritchie, N. Barberan, and J. Inkson, Phys. Rev. B **23**, 6486 (1981).
[46] W. Kohn and L. J. Sham, Phys. Rev. **140**, A1133 (1965).
[47] E. K. U. Gross and W. Kohn, Adv. Quantum Chem. **21**, 255 (1990).
[48] A. G. Eguiluz, Phys. Rev. Lett. **51**, 1907 (1983).
[49] A. Liebsch, Phys. Rev. B **36**, 7378 (1987).
[50] X.-M. Tong and Shih-I. Chu, Phys. Rev. A **55**, 3406 (1997).
[51] P. M. Echenique, R. M. Nieminen, and R. H. Ritchie, Solid State Commun. **37**, 779 (1981).

[52] I. Campillo, J. M. Pitarke and A. G. Eguiluz, Phys. Rev. B **58**, 10307 (1998).

[53] V. Olevano and L. Reining, Phys. Rev. Lett. **86**, 5962 (2001).

[54] A. Garcia-Lekue, J. M. Pitarke, E. V. Chulkov, A. Liebsch, and P. M. Echenique, Phys. Rev. B **68**, 045103 (2003).

[55] I. G. Gurtubay, J. M. Pitarke, and P. M. Echenique, Phys. Rev. B **69**, 245106 (2004).

[56] A. Liebsch, *Electronic Excitations at Metal Surfaces* (Plenum Press, New York, 1997) and references therein.

[57] A. Garcia-Lekue and J. M. Pitarke, Phys. Rev. B **64**, 035423 (2001).

[58] M. A. Cazalilla and F. J. Garcia de Abajo, Nucl. Instrum. Methods Phys. Res. B **125**, 106 (1997).

[59] J. M. Cowley, Surf. Sci. **114**, 587 (1982).

[60] Y. Fujii, S. Fujiwara, K. Narumi, K. Kimura, and M. Mannami, Nucl. Instrum. Methods Phys. Res. B **90**, 212 (1994).

[61] R. H. Ritchie, Phys. Rev. **114**, 644 (1959).

[62] P. Nozieres and D. Pines, *The Theory of Quantum Liquids* (Addision-Wesley, New York, 1990).

[63] E. P. Wigner, Phys. Rev. **46**, 1002 (1934).

[64] F. J. Garcia de Abajo and P. M. Echenique, Phys. Rev. B **46**, 2663 (1992).

[65] C. O. Reinhold and J. Burgdörfer, Phys. Rev. A **55**, 450 (1997).

[66] D. M. Newns, Phys. Rev. B **1**, 3304 (1970).

[67] T. L. Ferell, P. M. Echenique, and R. H. Ritchie, Solid State Commun. **32**, 419 (1979).

[68] J. Lindhard, K. Dans, K. Dan. Vidensk. Selsk. Mat. Fys. Medd. **28**, 8 (1954).

[69] R. H. Ritchie and A. Howie, Philos. Mag. **36**, 463 (1977).

[70] R. H. Ritchie, R. N. Hamm, J. E. Turner, H. A. Wright, and W. E. Bloch, Basic Life Sci. **58**, 99 (1992).

[71] B. W. Ninham, C. J. Powell, and N. Swanson, Phys. Rev. **145**, 209 (1966).

[72] P. Zacharias, J. Phys. F: Met. Phys. **5**, 645 (1975).

[73] K. Tőkési, X-M. Tong, C. Lemell, and J. Burgdörfer, Adv. Quantum Chem. **46**, 29 (2004).

[74] A. Liebsch, Phys. Rev. B **55**, 13263 (1997).

[75] J. Harris and A. Griffin, Phys. Lett. **34A**, 51 (1971).

[76] P. J. Feibelman, Phys. Rev. Lett. **30**, 975 (1973).

[77] P. J. Feibelman, Phys. Rev. B **9**, 5077 (1974).

[78] P. J. Feibelman, Prog. Surf. Sci. **12**, 287 (1982).

[79] S. Ichimaru, Rev. Mod. Phys. **54**, 1017 (1982).

[80] K. Tőkési, X.-M. Tong, C. Lemell, and J. Burgdörfer (unpublished).

[81] K. Tőkési and J. Burgdörfer, Surf. Sci. **454–456**, 1038 (2000).

[82] R. J. Warmack, R. S. Becker, V. E. Anderson, R. H. Ritchie, Y. T. Chu, J. Little, and T. L. Ferrell, Phys. Rev. B **29**, 4375 (1984).

[83] K. C. Mamola, R. J. Warmack, and T. L. Ferrell, Phys. Rev. B **35**, 2682 (1987).